Chinese Chemical Letters 37 (2026) 111756

Contents lists available at ScienceDirect

Chinese Chemical Letters

journal homepage: www.elsevier.com/locate/cclet

One-step synthesis of trimetallic PdCuNi porous nanoflowers for enhanced alcohol oxidation

Xinyu Gu[a], Jun Yu[a], Huiyu Sun[a], Nannan Zhang[a], Zhengying Wu[b,*], Yukou Du[a,*]

[a] College of Chemistry, Chemical Engineering and Materials Science, Soochow University, Suzhou 215123, China
[b] Jiangsu Key Laboratory for Environment Functional Materials, School of Materials Science and Engineering, Suzhou University of Science and Technology, Suzhou 215009, China

ARTICLE INFO

Article history:
Received 28 June 2025
Revised 15 August 2025
Accepted 25 August 2025
Available online 26 August 2025

Keywords:
PdCuNi
Porous structures
Ethanol and ethylene glycol oxidation
Trimetallic nanoalloy
One-step method

ABSTRACT

The three-dimensional (3D) Pd-based nanoflower structures, assembled from two-dimensional (2D) nanosheets, are characterized by their stable and ordered configurations. These structures have been extensively designed as anode materials for fuel cells. However, the exploration of trimetallic nanoflowers with porous architectures remains limited. In this study, we present a straightforward one-step solvothermal method for the synthesis of trimetallic PdCuNi porous nanoflowers (PNFs). Leveraging several unique advantages, such as an open superstructure, high porosity, and enhanced electronic interactions among the trimetals, the resulting PdCuNi PNFs demonstrate significantly improved electrochemical performance, with mass activities reaching 5.94 and 10.14 A/mg for the ethanol oxidation reaction (EOR) and the ethylene glycol oxidation reaction (EGOR), respectively. Furthermore, the PdCuNi PNFs exhibit optimized d-band centers and the most negative onset oxidation potential, indicating enhanced antitoxicity and stability. This study not only provides a novel perspective on the synthesis of 3D porous nanomaterials but also highlights the potential application value of trimetallic nanoalloys in catalysis.

© 2025 Published by Elsevier B.V. on behalf of Chinese Chemical Society and Institute of Materia Medica, Chinese Academy of Medical Sciences.

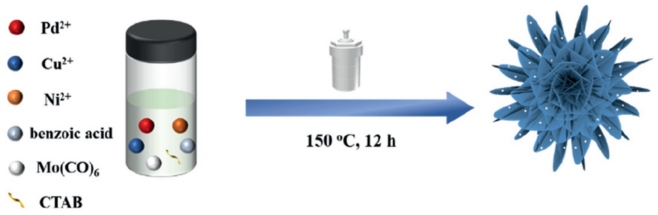
Direct alcohol fuel cells (DAFCs) represent an emerging and sustainable energy conversion technology, which promises to replace traditional fossil fuels [1,2]. This innovative system offers distinct advantages including rapid low-temperature start-up, environmental friendliness and simple structure [3–6]. However, the sluggish kinetics of the anodic oxidation reaction significantly hinder its commercialization [7–9]. Pt-based catalysts can effectively catalyze alcohol oxidation reaction (AOR), while the scarce reserves and easy-to-poisoning issues limit practical application [10–13]. Notably, Pd, with similar electronic structure and lattice parameters to Pt, can also deliver superior activity in alkaline AOR [14–17]. Therefore, a variety of strategies have been proposed to stimulate the catalytic potential of Pd nanomaterials [18–21].

The addition of one or two transition metals to form Pd-based nanoalloy has been validated as an effective strategy in a large number of practices [22–24]. On one hand, alloying can cut down the Pd usage and increase Pd atom utilization while maintaining activity through synergistic effects [25,26]. On the other hand, transition metals can weaken the adsorption of toxic species like CO and provide OH^- adsorption sites, facilitating oxidative removal of toxic species [27–29]. Among transition metals, Cu and Ni excel because they effectively promote C–C and C–H bond cleavage and the generation of oxygen species [30–32]. Especially the simultaneous introduction of Cu and Ni creates strong multi-component synergy and electronic interaction, significantly boosting electrocatalytic activity and stability [33]. For instance, Wang *et al.* prepared PdCuNi ternary alloys *via* wet-chemical methods, which showed exceptional oxygen reduction activity and remarkable methanol tolerance [34]. Therefore, rational introduction of Cu and Ni is crucial for constructing high-efficiency Pd-based ternary alloy catalysts for alcohol oxidation.

Moreover, the microstructure of catalyst plays a crucial role in electrocatalysis [35–37]. The 3D nanoflower structures assembled from 2D nanosheets, featuring open structure and abundant active sites, have triggered extensive research [38–40]. As a representative example, Zhang *et al.* developed a surfactant-free strategy for preparing ordered and stable 3D self-assembled nanosheet electrocatalysts [41]. However, most reported 3D nanoflowers display smooth surfaces, lacking additional porous architectures that accelerate mass transport and electron conduction [37]. Precisely engineering 3D nanoflowers with porous structures would significantly enhance anodic AOR kinetics and oxidation activity.

* Corresponding authors.
E-mail addresses: zywu@mail.usts.edu.cn (Z. Wu), duyk@suda.edu.cn (Y. Du).

https://doi.org/10.1016/j.cclet.2025.111756
1001-8417/© 2025 Published by Elsevier B.V. on behalf of Chinese Chemical Society and Institute of Materia Medica, Chinese Academy of Medical Sciences.



Scheme 1. Schematic of the synthetic procedure for the PdCuNi PNFs.

In this contribution, we propose an effective one-step method for constructing 3D PdCuNi nanoflowers that self-assembled from 2D nanosheets, characterized by their densely porous features. This porous structure provides enhanced pathways for mass transport and electron transfer. More importantly, the synergistic effect of Cu and Ni effectively tunes the electronic structure of Pd, mitigating the issue of Pd catalysts being prone to deactivation during electrochemical tests. Consequently, due to the aforementioned advantages, the mass activities of the PdCuNi PNFs in the ethanol and ethylene glycol oxidation reaction are found to be as high as 5.94 and 10.14 A/mg, significantly surpassing those of bimetallic PdCu PNFs, PdNi NFs and monometallic Pd/C. In addition to high activity, the PdCuNi PNFs also exhibit remarkable stability and excellent tolerance to poisoning species. This study not only presents a simple and straightforward scheme for constructing porous nanostructures but also confirms the reliable potential of trimetallic nanoalloy for electrocatalytic alcohol oxidation.

Scheme 1 illustrates the synthesis of PdCuNi PNFs by direct reduction of Pd, Cu and Ni precursors, using CTAB and benzoic acid as surfactant and structure-directing agent, with $Mo(CO)_6$ as reducing agent. First of all, the microstructure of the PdCuNi catalyst was characterized by high-angle annular dark-field scanning transmission electron microscopy (HAADF-STEM) and TEM. As presented in Figs. 1a and b, the PdCuNi PNFs exhibit a typical 3D nanoflower structure self-assembled from layered nanosheets. Notably, the nanoflowers possess abundant porous structures distributed throughout both interior and edge regions (Fig. 1c), which

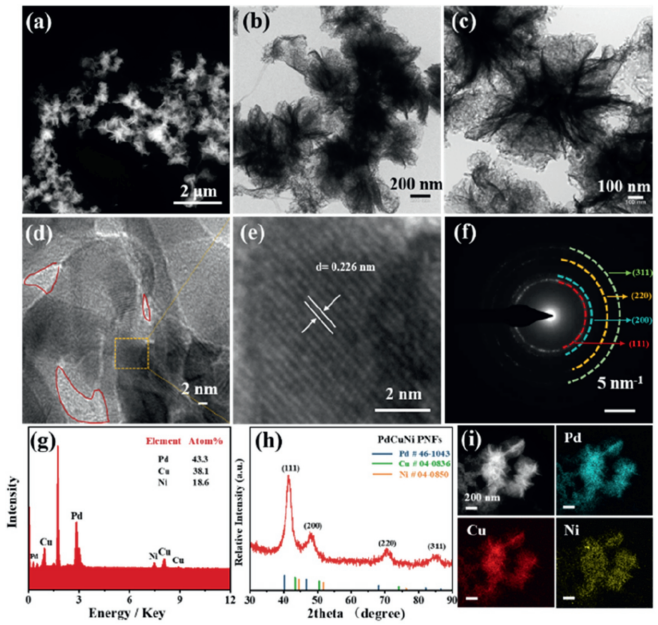


Fig. 1. Typical (a) HAADF-STEM image, (b, c) TEM image, (d, e) HRTEM image, (f) SAED, (g) SEM-EDS spectrum, (h) XRD pattern and (i) elemental mapping analysis of the PdCuNi PNFs.

substantially increase the specific surface area to provide more active sites for reactant adsorption [42,43]. Meanwhile, the dense pores also offer additional channels for electron transport [37]. In addition, the pores exhibit an irregular configuration as observed by high resolution TEM (HRTEM) (Fig. 1d). Fig. 1e reveals lattice fringes with a measured interplanar spacing of 0.226 nm, slightly smaller than that of the pure Pd (111) plane, indicating lattice contraction induced by the arrival of Cu and Ni. The atomic ratios of Pd, Cu and Ni in PdCuNi PNFs was measured as 40.1/36.9/23.0 by inductively coupled plasma mass spectrometry (ICP-MS) (Table S1 in Supporting information). Scanning electron microscopy energy-dispersive X-ray spectrometer (SEM-EDS) determined that the surface atomic ratio of Pd, Cu and Ni in PdCuNi PNFs was 43.3/38.1/18.6. (Fig. 1g). Thus, the Ni content in the bulk phase is slightly higher than that on the surface. The X-ray diffraction (XRD) pattern of PdCuNi is depicted in Fig. 1h, with diffraction peaks positioned between standard Pd (PDF #46–1043), Cu (PDF #04–0836), and Ni (PDF #04–0850), indicating the formation of a highly crystalline PdCuNi alloy [44]. The four peaks are indexed to the (111), (200), (220), and (311) planes of face-centered cubic (fcc) Pd. Elemental mapping images reveal the spatially uniform distribution of Pd, Cu, and Ni throughout the suface of PNFs (Fig. 1i), further verifying the formation of the ternary alloy. Moreover, the excellent crystallinity of the material is further confirmed by selected area electron diffraction (SAED), as the pattern display well-defined diffraction rings (Fig. 1f) [2]. The diffraction rings from the inner to the outer correspond to the (111), (200), (220), and (311) crystal planes, respectively.

PdCu PNFs and PdNi NFs were synthesized by omitting the Ni and Cu precursors, respectively, while keeping other conditions unchanged. TEM images reveal that PdCu PNFs exhibit layered porous nanoflower structures analogous to those of PdCuNi PNFs, with the majority of pores localized in the edge regions (Fig. S1a in Supporting information). In contrast, the PdNi NFs diaplay a smooth and flat surface without obvious pore distribution (Fig. S1d in Supporting information). The atomic ratios of Pd/Cu and Pd/Ni were determined to be 53.6/46.4 and 49.9/50.1 by ICP-MS (Table S1 in Supporting information), respectively. In the XRD patterns (Figs. S1c and f in Supporting information), the positions of the diffraction peaks shift relative to standard Pd and Cu/Ni, implying the presence of alloy structures [45,46].

Moreover, X-ray photoelectron spectroscopy (XPS) analysis reveals the surface valence state distribution and electron transfer behavior of as-prepared samples [47]. In Fig. 2a, the XPS spectra of the Pd 3d orbitals indicate that the valence states of Pd among these three substances are Pd(0) and Pd(II), with the former accounting for the major proportion. For PdCuNi PNFs, two prominent peaks at the binding energies (BEs) of 335.57 and 340.87 eV are identified as Pd(0) $3d_{5/2}$ and Pd(0) $3d_{3/2}$, respectively. Two minor peaks observed at 336.43 and 341.70 eV correspond to Pd(II) $3d_{5/2}$ and Pd(II) $3d_{3/2}$, respectively. Meanwhile, it can be detected that the Pd(0) 3d BEs of PdCuNi PNFs display a positive shift of 0.57 eV compared to the standard values (335.00 and 340.30 eV). Similarly, the BEs of Ni(0) $2p_{3/2}$ and $2p_{1/2}$ in PdCuNi PNFs (853.17 and 870.60 eV) show a positive shift relative to those of standard Ni (852.60 and 869.90 eV) (Fig. 2c). However, the BEs of Cu $2p_{3/2}$ and $2p_{1/2}$ (932.17 and 952.03) are negatively shifted in comparison with those of standard Cu (Fig. 2b). These BE shifts indicate the presence of electronic interactions among Pd, Cu, and Ni. Specifically, electrons flow from Pd and Ni to Cu. This electron transfer effectively modifies the electronic structure of Pd and enhances its catalytic performance [48]. Further, the XPS spectra of elements in PdCuNi PNFs are compared with those in PdCu PNFs and PdNi NFs. It is obvious that the BEs of the metallic states of Pd, Cu and Ni in PdCuNi PNFs are shifted relative to those in PdCu PNFs and PdNi NFs, further confirming electron transport between Pd, Cu and Ni.

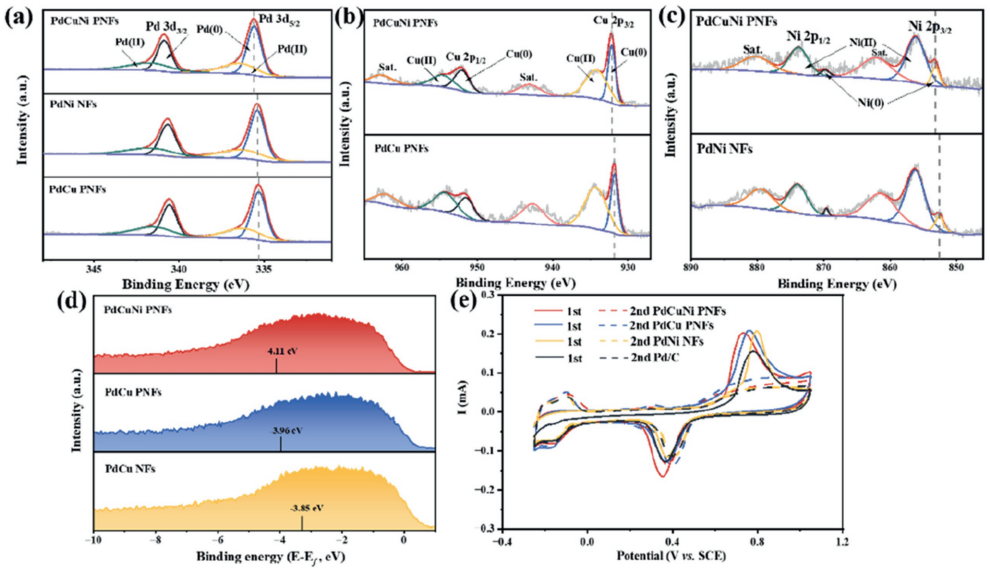


Fig. 2. (a) XPS spectra of Pd 3d in PdCuNi PNFs, PdCu PNFs and PdNi NFs. (b) XPS spectra of Cu 2p in PdCuNi PNFs and PdCu PNFs. (c) XPS spectra of Ni 2p in PdCuNi PNFs and PdNi NFs. (d) The valence band spectra. (e) CO stripping voltammograms.

Since the Cu 2p binding energies of Cu(0) and Cu(I) overlap, LMM Auger spectra was adopted to correctly distinguish between them in the sample. Cu(0) LMM peaks typically appear at the kinetic energy of 918.4 eV and Cu(I) at 916.5 eV [49]. As shown in Figs. S2a and b (Supporting information), a prominent LMM peak is observed at 918.6 eV, consistent with Cu(0), with no characteristic Auger peak Cu(I) near 916.5 eV. For Cu(II) identification, the Cu 2p XPS spectra of PdCuNi PNFs and PdCu PNFs show peaks at about 934 and 954 eV, accompanied by satellite peaks at about 943 and 963 eV. Since no Cu(I) signals are detected, it is reasonable to conclude that surface Cu species are dominated by metallic Cu and CuO. Finally, most Ni exists in the oxidized state, and only a small portion is in the metallic state. This phenomenon can be attributed to the strong oxygenophilicity of Ni and the surface sensitivity of XPS characterization [50].

The valence band spectra (VBS) can reveal the d-band center metals, thereby providing insights into the adsorption/desorption strength of intermediate species [37]. Fig. 2d displays that the PdCuNi PNFs present a d-band center of −4.11 eV, an apparent downshift relative to that of PdCu PNFs (−3.96 eV) and PdNi NFs (−3.85 eV). The downward shift of the d-band centre in PdCuNi PNFs can attenuate the strong adsorption of toxic intermediates (*e.g.*, CO) and liberate blocked active sites. Furthermore, CO stripping experiments were conducted to evaluate the poisoning resistance against CO of each sample [51]. As depicted in Fig. 2e, PdCuNi PNFs exhibit the most negative onset potential compared with PdCu PNFs, PdNi NFs and Pd/C. A more negative potential signifies easier CO oxidative desorption, and superior anti-poisoning performance. Therefore, based on the analysis of the VBS and CO stripping experiments, it can be concluded that the PdCuNi PNFs possess remarkable CO tolerance capability. This might stem from that the strong electronic structure regulation ability of the trimetal system, prompting the main catalytic metal Pd to exert greater catalytic potential [52].

The electrochemical performance of PdCuNi PNFs towards EOR was evaluated in alkaline solution, with PdCu PNFs, PdNi NFs, and Pd/C serving as comparative catalysts for parallel investigation. The electrochemical active surface area (ECSA) is an important performance metric, obtained from the area of the reduction peak in the cyclic voltammetry (CV) curves measured in 1 mol/L KOH solution (Fig. 3a). The ECSA values of PdCuNi PNFs, PdCu PNFs, PdNi NFs and Pd/C are 42.81, 40.96, 42.47 and 25.06 m^2/g_{Pd}, respectively. The PdCuNi PNFs exhibit the highest ECSA value, suggesting that the trimetallic porous nanostructure provides massive active sites during electrochemical reactions [32]. Subsequently, the CV curves tested in 1 mol/L KOH and 1 mol/L ethanol solution were recorded and normalized by mass for the most intuitive assessment of the EOR performance of four catalysts. The forward peak at approximately −0.22 V arises from the oxidation of ethanol molecules, and the reverse peak at −0.35 V results from the further oxidation of strongly adsorbed species [31]. The results (Fig. 3b) reveal that PdCuNi PNFs display outstanding electrocatalytic activity of 5.94 A/mg, approximately 1.42 times higher than that of PdCu PNFs (4.18 A/mg), 1.9 times that of PdNi NFs (3.12 A/mg), and 4.37 times that of commercial Pd/C (1.36 A/mg). The specific activity maintains the identical ranking order: PdCuNi PNFs (13.87 mA/cm^2) > PdCu PNFs (10.20 mA/cm^2) > PdNi NFs (7.35 mA/cm^2) > Pd/C (5.44 mA/cm^2) (Fig. 3c). Meanwhile, the ethanol oxidation activity of PdCuNi PNFs also show remarkable advantages over recent Pd-based nanomaterials (Table S2 in Supporting information). Thus, the synergistic effects among the trimetallic components profoundly optimize the electrocatalytic ethanol oxidation activity [53]. Moreover, the porous structure plays an important role in enhancing the EOR performance. On one hand, the porous structure confers PdCuNi PNFs with an enlarged surface area and abundant low-coordination surface atoms, thereby increasing the number of active sites [23]. On the other hand, the pores can provide transport channels for reactants and charges, facilitating their access to the active sites, thus enhancing the reaction rate [37]. The onset potentials derived from the CV curves are compared to probe the reaction kinetic (Fig. 3d). Compared with commercial Pd/C, the onset potentials of PdCuNi PNFs, PdCu PNFs, and PdNi NFs exhibit negative shifts of 84, 5, and 67 mV, respectively, indicative of accelerated electrode reaction kinetics for the PdCuNi catalyst. The CV curves at different scan rates were employed to further evaluate the electrochemical kinetics (Fig. 3e and Fig. S3 in Supporting information). Fig. 3f depicts mass activity (j) follows a linear relationship with the square root of the scan rate ($v^{1/2}$), and the PdCuNi electrode delivers the largest slope among all these studied electrodes. This result indicates that the PdCuNi PNFs electrode possesses a higher transport electron coefficient during the kinetic process, markedly boosting the overall EOR efficiency.

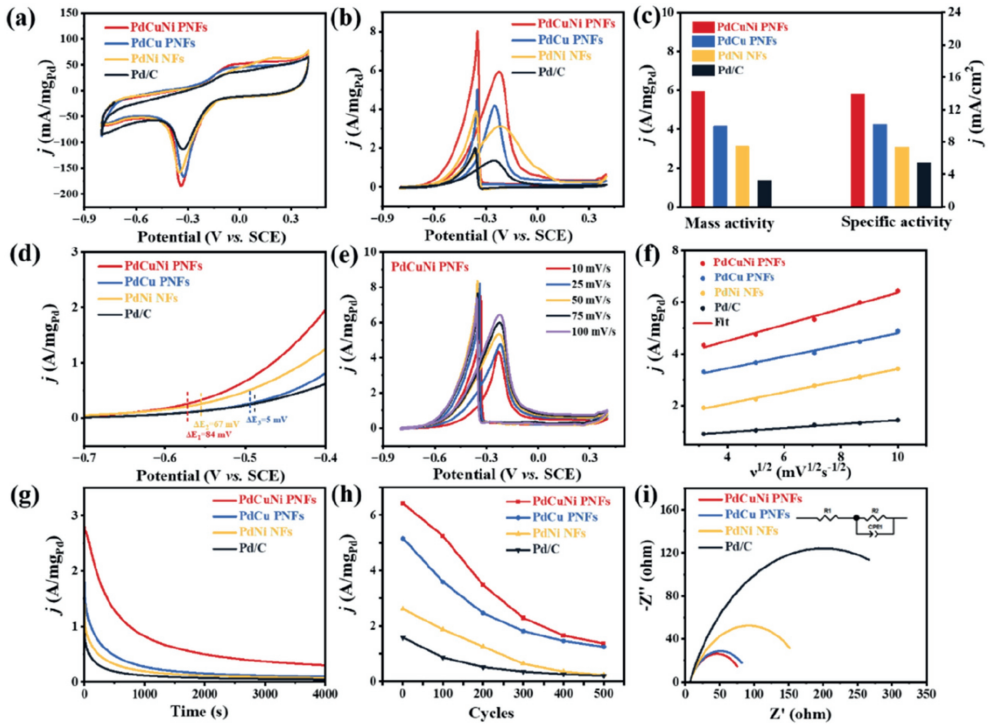


Fig. 3. The EOR performances of PdCuNi PNFs, PdCu PNFs, PdNi NFs and commercial Pd/C. CV curves in (a) 1 mol/L KOH solution and (b) 1 mol/L KOH containing 1 mol/L ethanol electrolyte. (c) The histogram of mass activity and specific activity. (d) Onset potentials. (e) CV curves of PdCuNi PNFs at different scan rates. (f) The plot of mass activity *vs*. the square root of the scan rate. (g) CA curves at −0.24 V. (h) The variation of mass activity along with 500 cycles. (i) EIS spectra.

Another critical requirement for DAFCs is the long lifespan of anode catalysts. First, the chronoamperometry (CA) tests were conducted to investigate the changes in their current density over time. As depicted in Fig. 3g, the oxidation current of all catalysts declines gradually with time during ethanol electrooxidation, primarily due to the accumulation of intermediate products [35]. Strikingly, the PdCuNi PNFs display the slowest current density loss and sustain the highest activity (0.30 A/mg) after 4000 s. In contrast, the current densities of PdCu PNFs, PdNi NFs, and commercial Pd/C suffer rapid decline and retain only 0.092, 0.069 and 0.043 A/mg, respectively, over the same period. Subsequently, we performed consecutive 500 CV cycles and recorded the remaining mass activity of the catalyst every 100 cycles (Fig. 3h and Fig. S4 in Supporting information). After 500 cycles, the PdCuNi PNFs still maintain a residual mass activity of 1.36 A/mg, outperforming all other comparative catalysts. Therefore, the PdCuNi PNFs demonstrate optimal stability and the desired enhancement can stem from the introduction of the third metal. This incorporation further modulates the electronic structure of active sites and mitigates catalyst deactivation caused by excessively strong adsorption of toxic species in single metal or bimetal systems [54]. In addition, the electrochemical impedance spectroscopy (EIS) was adopted to further measure the interfacial charge transfer resistance [55,56]. The PdCuNi catalyst exhibits an apparently smaller impedance arc diameter (DIA) and lower charge transfer resistance (R_{ct}) value (Fig. 3i and Table S3 in Supporting information), thus enabling more rapid interfacial reaction kinetics.

The capacity of PdCuNi catalysts for ethylene glycol oxidation under alkaline conditions was investigated by the same method. Fig. 4a depicts the PdCuNi PNFs achieve the highest mass activity value of up to 10.14 A/mg, followed by PdCu PNFs (6.54 A/mg), PdNi NFs (5.51 A/mg) and commercial Pd/C (1.84 A/mg) electrodes. The PdCuNi PNFs remarkable EGOR performance can be ascribed to the porous structure that exposes more catalytically active sites and the co-modification by Cu and Ni that optimizes the Pd electronic structure and enhances its intrinsic catalytic capability [32,57]. Similarly, the PdCuNi PNFs electrode reaches a maximum specific activity value of 23.69 mA/cm^2 (Fig. 4b), and the value is found to be about 1.48, 1.83, and 3.21 times as large as those of the PdCu PNFs (15.97 mA/cm^2), PdNi PNFs (12.97 mA/cm^2), and Pd/C (7.37 mA/cm^2) electrodes, respectively. In addition, the ethylene glycol oxidation activity of PdCuNi PNFs is also more competitive compared with that of recent Pd-based nanocatalysts (Table S4 in Supporting information). As depicted in the enlarged CV curves (Fig. 4c), the PdCuNi electrode achieves the same EG oxidation current at a lower potential than other electrodes, implying that the presence of the PdCuNi PNFs catalyst makes the catalytic reaction proceed more easily. For consistent evaluation, the CA tests were utilized to compare the stability of PdCuNi PNFs with that of other electrodes (Fig. 4d). The data reveals the PdCuNi PNFs electrode could maintain considerable mass activity after 4000 s, with residual activities of 1.05, 0.43, 0.36, and 0.17 A/mg for PdCuNi PNFs, PdCu PNFs, PdNi NFs, and Pd/C, respectively. This confirms that the porous structure and the alloy effect of Pd, Cu and Ni are conducive to sustaining the EGOR activity [58]. Furthermore, the PdCuNi PNFs also display a distinct advantage in continuous 500 CV tests with a lower attenuation rate of mass activity compared with PdCu PNFs, PdNi NFs and Pd/C electrodes (Fig. 4e and Fig. S5 in Supporting information). The result further confirms that the PdCuNi PNFs catalyst is highly effective in extending the service life. Finally, the DIA and R_{ct} value of the PdCuNi PNFs electrode are much smaller than those of other catalyst electrodes (Fig. 4f and Table S5 in Supporting information), indicating that Cu and Ni greatly promote electron transfer and mass transport.

In summary, a robust co-reduction approach is successfully developed for the fabrication of 3D PdCuNi porous nanoflower catalysts. The resulting structure exhibits layered porous features, low coordinated sites, a strong trimetallic synergistic effect, a lower

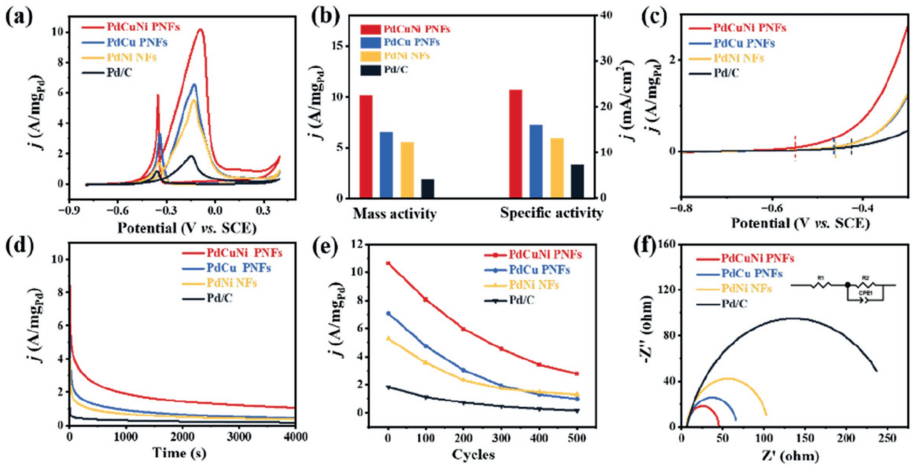


Fig. 4. The EGOR performances of PdCuNi PNFs, PdCu PNFs, PdNi NFs and commercial Pd/C. (a) CV curves. (b) Summarized mass activity and specific activity. (c) Onset potentials. (d) CA curves at −0.13 V. (e) The long-term variation of activity with cycles. (f) EIS spectra.

d-band center and excellent conductivity. Collectively, these characteristics significantly enhance the electrocatalytic process for ethanol and ethylene glycol oxidation reactions. Consequently, exceptional electrocatalytic capabilities have been achieved for PdCuNi PNFs, including higher ECSA values, a mass activity of up to 5.94 A/mg and 10.14 A/mg for EOR and EGOR, respectively. The PdCuNi PNFs catalyst also demonstrates more prominent reaction kinetics, and superior stability and resistance to toxicity. It is believed that this simple co-reduction strategy can be easily extended for the design and synthesis of other trimetallic porous nanoflowers, holding broad application promise in organic small molecule catalysis.

Declaration of competing interest

The authors declare that they have no known competing financial interests or personal relationships that could have appeared to influence the work reported in this paper.

CRediT authorship contribution statement

Xinyu Gu: Writing – original draft, Methodology, Investigation, Conceptualization. **Jun Yu:** Writing – review & editing, Methodology, Investigation. **Huiyu Sun:** Writing – review & editing, Supervision. **Nannan Zhang:** Writing – review & editing. **Zhengying Wu:** Writing – review & editing. **Yukou Du:** Supervision, Resources, Funding acquisition.

Acknowledgment

This work was supported by the National Natural Science Foundation of China (No. 52274304).

Supplementary materials

Supplementary material associated with this article can be found, in the online version, at doi:10.1016/j.cclet.2025.111756.

References

[1] K.L. Wang, P.C. Liu, M.Z. Wang, et al., Chin. Chem. Lett. 36 (2025) 110532.
[2] Y. Zhao, L.K. Yang, J.L. Li, et al., Inorg. Chem. 64 (2025) 5960–5970.
[3] J.F. Chang, G.Z. Wang, C. Li, et al., Joule 7 (2023) 587–602.
[4] B.Q. Miao, B. Sun, T.J. Wang, et al., Appl. Catal. B: Environ. Energy 337 (2023) 122967.
[5] Y. Sun, H.Y. Xiang, H.M. Li, et al., Chin. Chem. Lett. 31 (2020) 2491–2494.
[6] F. Chen, Q. Zhou, S.Y. Yu, et al., J. Colloid Interface Sci. 692 (2025) 137488.
[7] W.Y. Zhang, Y. Yang, B.L. Huang, et al., Adv. Mater. 31 (2019) 1805833.
[8] F.M. Li, C.F. Xia, W.S. Fang, Y. Chen, B.Y. Xia, Adv. Energy Mater. 14 (2024) 2400112.
[9] J. Ma, B. Liu, R.Y. Wang, et al., Chin. Chem. Lett. 33 (2022) 2585–2589.
[10] K. Bhunia, K.S. Bejigo, S.J. Kim, Chem. Eng. J. 484 (2024) 149306.
[11] L.Y. Jiang, F.M. Tian, X.Y. Chen, et al., J. Colloid Interface Sci. 649 (2023) 118–124.
[12] F.L. Zhao, Q. Yuan, Inorg. Chem. 62 (2023) 14815–14822.
[13] J.J. Ding, S.J. Jing, C.Q. Yin, et al., Chin. Chem. Lett. 34 (2023) 107899.
[14] A.P. Chandran, S. Mondal, D. Goud, et al., Adv. Mater. 37 (2025) 2415362.
[15] S. Kitano, H. Motohashi, M. Iwai, et al., Appl. Surf. Sci. 670 (2024) 160552.
[16] Y. Jin, J.D. Chen, R.J. Li, et al., Appl. Surf. Sci. 648 (2024) 159093.
[17] C. Chen, X.Z. Lao, J.L. Li, et al., ACS Appl. Mater. Interfaces 17 (2024) 3308–3315.
[18] Z.L. Qin, A.L. Fan, Q. Zeng, ACS Appl. Energ. Mater. 6 (2023) 5607–5615.
[19] K.W. Zhang, C. Wang, F. Gao, et al., Coord. Chem. Rev. 472 (2022) 214775.
[20] G.L. Zhang, C.Y. Hui, Z.Z. Yang, et al., Appl. Catal. B: Environ. Energy 342 (2024) 123377.
[21] Y.P. Zhang, F. Gao, H.M. You, et al., Coord. Chem. Rev. 450 (2022) 214244.
[22] J. Li, Y.H. Xu, C. Wang, et al., Surf. Interf. 42 (2023) 103360.
[23] J. Yu, J.W. Hong, Appl. Surf. Sci. 659 (2024) 159903.
[24] A. Sathyaseelan, V. Elumalai, K. Krishnamoorthy, A. Sajeev, S.J. Kim, ACS Sustain. Chem. Eng. 11 (2023) 5345–5355.
[25] A.M. Alamer, M.Y. Ouyang, F.H. Alshafei, et al., ACS Catal. 13 (2023) 9987–9996.
[26] M.Y. Hu, J. Li, Z.Y. Wu, Y.K. Du, Surf. Interf. 44 (2024) 103755.
[27] W.H. Guo, X.Z. Yao, L.Y. Peng, et al., Chin. Chem. Lett. 31 (2020) 836–840.
[28] X.H. Tan, C.H. Wang, J.R. Wang, et al., Adv. Sci. 11 (2024) 2409109.
[29] Y. Liu, H. Gao, F.J. Meng, et al., ACS Appl. Mater. Interfaces 17 (2025) 25713–25721.
[30] J.M. Xu, X.W. Guo, Y.J. Guan, P. Wu, Chin. Chem. Lett. 33 (2022) 349–353.
[31] X.Y. Gu, D.Q. Wang, N.N. Zhang, et al., J. Colloid Interface Sci. 677 (2025) 750–757.
[32] D.Q. Wang, Y.P. Zhang, K.W. Zhang, et al., J. Colloid Interface Sci. 650 (2023) 350–357.
[33] J.W. Wang, Y.W. Ling, H.L. Yan, X.X. Li, ChemNanoMat 8 (2022) e202200290.
[34] H.W. Wang, W.J. Luo, L.J. Zhu, et al., Adv. Funct. Mater. 28 (2018) 1707219.
[35] N.N. Zhang, J. Li, W.Y. Liang, et al., Inorg. Chem. 63 (2024) 7063–7070.
[36] X.Y. Zhao, H.C. Zhao, J.F. Sun, G. Li, R. Liu, Chin. Chem. Lett. 31 (2020) 1782–1786.
[37] T.N. Zhang, Y.C. Cao, H.N. Zheng, et al., ACS Sustain. Chem. Eng. 13 (2025) 1993–2000.
[38] S.Y. Liu, Y. Zhao, Y.D. Wang, J. Yan, P.Z. Guo, ChemCatChem 17 (2025) e202500303.
[39] F. Gao, Y.P. Zhang, F.F. Ren, Y. Shiraishi, Y.K. Du, Adv. Funct. Mater. 30 (2020) 2000255.
[40] L.J. Jin, H. Xu, C.Y. Chen, et al., ACS Appl. Mater. Interfaces 11 (2019) 42123–42130.
[41] K.W. Zhang, C. Wang, H.M. You, et al., Chem. Eng. J. 438 (2022) 135666.
[42] H. Fu, Z. Huang, T. Zhu, et al., ACS Mater. Lett. 6 (2024) 4801–4809.
[43] Z. Liu, X.H. Ge, Q.H. Guan, et al., Appl. Surf. Sci. 654 (2024) 159534.
[44] Y.X. Wang, C.F. Liu, M.L. Yang, et al., Chin. Chem. Lett. 28 (2017) 60–64.
[45] G.H. Han, J.Y. Seo, M. Kang, et al., J. Energy Chem. 93 (2024) 8–15.
[46] D. Wang, Z. Chen, Y. Wu, et al., SmartMat 4 (2022) e1117.
[47] Y.K. Lv, Y. Han, K. Wang, et al., ACS Nano 18 (2024) 32186–32195.
[48] G. Fisseha, Y.P. Hu, Y.N. Yu, et al., Chin. Chem. Lett. 35 (2024) 108445.

[49] Z. Cao, Z.Q. Ouyang, Z.Y. Liu, et al., Appl. Surf. Sci. 560 (2021) 150021.
[50] M.Y. Mao, J. Wu, Y. Wang, Y. Long, G.Y. Fan, Appl. Surf. Sci. 600 (2022) 153988.
[51] J. Li, Y.F. Zhang, C.Q. Ye, Y.K. Du, Inorg. Chem. 64 (2025) 2118–2126.
[52] K. Liu, H.P. Huang, Y.X. Zhu, et al., J. Mater. Chem. A 10 (2022) 3808–3817.
[53] Q.Y. Li, X.X. Zhou, M.N. Lu, et al., J. Colloid Interface Sci. 653 (2024) 1264–1271.
[54] N.K. Qian, L. Ji, J.J. Li, H. Zhang, D.R. Yang, Nano Res. 16 (2023) 9125–9131.
[55] D.Q. Wang, Y.P. Zhang, Z.L. Li, et al., J. Colloid Interface Sci. 636 (2023) 602–609.
[56] J. Li, Y. Zhang, L. Zhang, et al., Angew. Chem. Int. Ed. 64 (2025) e202425006.
[57] F.L. Wang, C.W. Kuang, Z.C. Zheng, et al., Chin. Chem. Lett. 36 (2025) 109989.
[58] L. Zhang, Z.W. Zhao, X. Fu, et al., ACS Appl. Mater. Interfaces 15 (2023) 5198–5208.